1   **Electrokinetic delivery of reactants: pore water chemistry controls**

2   **transport, mixing and degradation**

3

4

5   Riccardo Sprocati[1], Andrea Gallo[2], Rajandrea Sethi[2], Massimo Rolle[1*]

6

7

8   [1]Department of Environmental Engineering, Technical University of Denmark,

9   Bygningstorvet, Building 115, 2800 Kgs. Lyngby, Denmark

10   [2]Department of Environmental, Land and Infrastructure Engineering, Politecnico di Torino,

11   Corso Duca degli Abruzzi 24, 10129 Torino, Italy

12

13   [*]Corresponding author phone: +45 45251566; email: masro@env.dtu.dk

14

15 **Abstract**

16 Electrokinetics in porous media entails complex transport processes occurring upon the

17 establishment of electric potential gradients, with a wide spectrum of environmental

18 applications ranging from remediation of contaminated sites to biotechnology. The resulting

19 electric forces cause the movement of pore water ions in opposite directions, leading to charge

20 interactions that can affect the distribution of charged species in the domain. Here, we

21 demonstrate that changes in chemical conditions, such as the concentration of a background

22 electrolyte in the pore water of a saturated porous medium, exert a key control on the

23 macroscopic transport of charged tracers and reactants. The difference in concentration

24 between the background electrolyte and an injected solute can limit or enhance the reactant

25 delivery, cause non-intuitive patterns of concentration distribution, and ultimately control

26 mixing and degradation kinetics. With non-reactive and reactive electrokinetic transport

27 experiments combined with process-based modeling, we show that microscopic charge

28 interactions in the pore water play a crucial role on the transport of injected plumes and on the

29 mechanisms and rate of both physical and chemical processes at larger, macroscopic scales.

30 Our results have important implications on electrokinetic transport in porous media and may

31 greatly impact injection and delivery strategies in a wide range of applications, including in

32 situ remediation of soil and groundwater.

33

36

Introduction

Electrokinetics in porous media has important applications in many different disciplines, as well as an enormous and yet unexplored potential. For instance, electrokinetics (EK) is used in microbial fuel cells[1–3], rapid tests of rocks and concrete[4,5], water purification[6–9] and may play an important role on enhanced and sustainable resources recovery[10–12]. An important environmental application of electrokinetic techniques is the remediation of soil and subsurface porous media[13–15], in which the use of low-intensity electric fields can lead to the mobilization of contaminants and to the effective delivery of reactants and amendments, including bacteria[16–19]. Particularly promising is the capability of electrokinetic processes to distribute reactants in impervious, low-permeability porous media, which are not accessible by hydraulic flushing and can represent long term sources of contamination for soils and groundwater resources[20–22]. An important feature for many subsurface applications is that EK empowers effective delivery and mobilization strategies through the transport mechanisms induced by the application of an electric potential gradient. Such mechanisms include electromigration, consisting in the movement of ions in opposite directions depending on their charge, electroosmosis, resulting in an advective flow caused by the movement of ions in proximity of the solid grains' surfaces, and electrophoresis, affecting the transport of charged particles[23]. Despite the large number of current and potential applications, the quantitative understanding of electrokinetic phenomena in porous media remains a daunting challenge due to the complexity of the controlling processes that depend on physical, chemical and electrical properties of both fluids and solid matrices.

Here, we focus on electromigration transport of charged solutes in saturated porous media and we experimentally demonstrate that the electrolyte composition of the pore water greatly impacts the macroscopic dynamics of electrokinetic transport. We consider permanganate (MnO_4^-) as a colored charged tracer due to its visible properties and its widespread use as strong

62   oxidant for the degradation of organic contaminants also in EK applications[24–27]. We show that

63   background electrolyte concentrations control the delivery of the injected MnO_4^-, its spatial

64   distribution and its mixing behavior with the surrounding pore water. Furthermore, in our

65   experiments we study reactive transport of MnO_4^-, oxidizing a non-charged organic solute

66   initially present in the porous domain. We illustrate the mechanism and impact of

67   electrokinetically-induced charge mixing, in which the concentration of the background

68   electrolyte affects both the extent of mixing and the kinetics of the mixing-controlled reaction.

69   The electrokinetic experiments are compared with transport by advection and dispersion: the

70   radically different dynamics of EK-induced transport and electrolyte-controlled reactions are

71   systematically analyzed with the support of process-based numerical simulations.

72

Materials and Methods

74   To evaluate the displacement mechanisms of a tracer under different conditions of advective-

75   dispersive and electrokinetic transport and to illuminate the role of charge interactions, we

76   designed a quasi-two-dimensional experimental setup, schematically illustrated in Figure S1a-

77   b (Supporting Information). The system consists of a tempered glass chamber (inner size 795

78   mm × 182 mm × 11 mm) held by an aluminum structure with an internal polyethylene layer.

79   The porous medium (glass beads, with grain size 0.40-0.60 mm, Sigmund Lindner, Germany)

80   was included in the central part of the system (300 mm × 180 mm × 11 mm), delimited by two

81   acrylic separators with honeycomb mesh and covered by a fabric layer.

82   For the advection-dispersion experiments (Figure S1a), recirculation between the reservoirs

83   was established to ensure the desired hydraulic gradient. The flow rate was controlled with a

84   high-precision, multi-channel peristaltic pump (ColeParmer, United States), and steady-state

85   conditions could be reached in few minutes. The pump was operated with 5 channels, providing

86   a constant seepage velocity in the porous medium of 6.5 cm/h.

87 For the EK experiments (Figure S1b), graphite rod electrodes (ø6×300 mm, Elektrokul,

88 Denmark) were placed in the glass chamber, in two reservoir zones outside the porous medium.

89 The distance between the two electrodes was 400 mm for all experiments. An electrolyte

90 solution was recirculated in two external reservoirs to provide additional volume to reduce the

91 impact of electrolysis reactions on the system pH. To recirculate water in the reservoirs, a four-

92 channel peristaltic pump (Ole Dich, Denmark) was operated with 2 channels, providing a

93 constant flowrate of 40 mL/min. The graphite electrodes were connected to a power supply

94 (EA Elektro-Automatik, EA-PSI 5200-10A, Germany) by means of electric wires. The voltage

95 provided by the power supply throughout the experiments was kept constant at 200 V. The

96 current in the system was measured by connecting the wire from the power supply to the anode

97 through a multimeter (PeakTech 3315, Germany). The effective potential drop within the

98 porous media was measured by means of two wire electrodes (exposed tip 2 mm) placed

99 centered in the setup, 10 mm below the water table and at a distance of 280 mm. The potential

100 reading was performed with a second digital multimeter (PeakTech 3315, Germany). Voltage

101 and current measurements were recorded with the multimeter at every hour of operation and

102 were found to be in a range 122.1-148.7 V and 3.0-24.8 mA, respectively. The values measured

103 in the different experiments are reported in the Supporting Information (Table S1).

104 Advection-dispersion and EK transport have been studied performing injections of potassium

105 permanganate ($KMnO_4$) on the left-side of the domain. To investigate the role of charge

106 interactions on the transport of ions, we performed first a set of conservative, non-reactive

107 experiments followed by a second set of reactive experiments, in which glucose (Sigma-

108 Aldrich, United States) was added to the background solutions to reach a concentration of 8

109 mol/m^3. For all experiments, the concentration of the injected $KMnO_4$ was constant (3 mol/m^3)

110 whereas the background electrolyte concentration, consisting in a solution with a fixed ratio of

111 $NaHCO_3$ and Na_2CO_3 to reach a pH of 9, was varied for the different investigated scenarios.

112 In all cases, the injected tracer solution displaces the background fluid and creates a circular

113 plume shape and a conductivity difference in the system.

114 The experiments were conducted in a dark room and the glass chamber was illuminated from

115 the back with an electroluminescent panel (1000 mm × 300 mm, EL-Technik, Germany) and

116 from the front with a light bulb (Philips 4000K, 806 lm, 100 mA, 9.5W). A calibration

117 procedure was developed to relate the color intensity of permanganate with its concentration

118 and to quantify the spatial distribution of the permanganate plumes in the porous medium at

119 different times. Details about the setup and the image analysis and calibration techniques are

120 provided in Supporting Information (Section S2).

121

122 **Theoretical background**

123 The transport of dissolved species in saturated porous media occurs as a result of concentration,

124 electric potential and pressure gradients. These phenomena result in diffusion/dispersion,

125 electromigration and advective fluxes, which are described by the Nernst-Planck equation[28–33]:

$$\boldsymbol{J}_i^{Tot} = \underbrace{-nD_i\nabla c_i}_{J_i^{Dif}} \underbrace{-nD_i\frac{z_iF}{RT}c_i\nabla\Phi}_{J_i^{Mig}} \underbrace{+n\boldsymbol{u}c_i}_{J_i^{Adv}} \tag{1}$$

126 where n is the porosity, c_i is the molar concentration, D_i is the pore diffusion/dispersion

127 coefficient, z_i is the charge number, Φ is the electric potential and $\boldsymbol{u}$ is the seepage velocity.

128 In absence of advective fluxes, transport by electromigration, provided sufficient electric

129 potential gradients, is the dominant component. Such situation is typical of electrokinetic

130 applications, in which the transport of ions by electromigration depends on the applied electric

131 potential, on the diffusive/dispersive properties and on the charge of the individual ions. This

132 makes anions and cations move in presence of an electric field in opposite directions, whereas

133 non-charged solutes are not affected by the applied voltage. Considering a porous medium,

134 ions in solution need to comply with the electroneutrality condition $\sum_{i=1}^{N} z_i c_i = 0$, which

135 corresponds to the Poisson's equation under the assumption of overall zero charge density in

136 the domain[34,35]. Given that ions in aqueous solutions have different diffusion coefficients

137 (Table S3, Supporting Information), under the application of an electric field they will move

138 with different electromigration velocities. Such properties, in combination with the

139 electroneutrality condition, imply that the electrokinetic transport of ions is affected by the

140 overall electrolyte composition of the system, thus making charge interactions play a key role

141 for the movement of the different charged species.

142 Considering that the application of an electric current in a porous medium results in a flux of

143 ions, it is possible to define the current density from the definition of total fluxes in Eq. 1. As

144 an external current can result in significant electric potential gradients, it is possible to assume

145 that the current density can be approximated as[28]:

$$\mathbf{I} = F \sum_{i=1}^{N} J_i^{Mig} z_i = F^2 \sum_{i=1}^{N} z_i^2 \frac{nD_i}{RT} c_i \nabla\Phi = \sigma_e \nabla\Phi \qquad (2)$$

146 Eq. 2 indicates that there are strong dependencies between the current density I and the

147 conductivity of the electrolyte solution σ_e. In particular, as σ_e changes in the system, the current

148 density and the electric potential gradient are also spatially and temporally variable in the

149 porous medium domain. Indeed, changes in electric potential gradients impact the intensity and

150 direction of migration fluxes, which ultimately affect the concentration and distribution of ionic

151 species in the system.

152 Process-based numerical modeling was performed with the codes NP-Phreeqc[36] and NP-

153 Phreeqc-EK[37] for the cases of advection-dispersion and electrokinetic transport, respectively.

154 These simulators are based on a coupling between COMSOL Multiphysics and the

155 geochemical code PhreeqcRM[38], operated through a MATLAB LiveLink interface. For

156 electrokinetic transport, NP-Phreeqc-EK solves the Nernst-Planck-Poisson equations in

157 multidimensional domains and is able to account for a wide range of equilibrium and

158   kinetically-controlled reactions. The coupling with the geochemical code accounts for the

159   composition and aqueous speciation of the pore water. The initial solution speciation for each

160   scenarios is reported in Tables S4 (Supporting Information).

161

162   **Results and discussion**

163   *Conservative transport experiments*

164   For the set of conservative experiments, the first scenario focuses on the movement of the

165   purple-colored permanganate ion (MnO_4^-) undergoing advective-dispersive transport induced

166   by a simple pressure head gradient and without applying any electric potential difference

167   between the electrodes (Figure 1). Three experimental scenarios were then dedicated to the

168   investigation of EK transport. In these experiments, the application of a constant electric

169   potential at the electrodes resulted in transport of the injected permanganate by

170   electromigration. The electric potential in the system was set to provide an electromigration

171   velocity comparable with the seepage velocity in the advective-dispersive experiment.

172   Therefore, the electromigration velocity of MnO_4^- in the system was approximately 6.5 cm/h.

173   The considered EK transport scenarios were characterized by three different electrolyte

174   concentrations of the background pore water solution. We refer to "EK equal" for the scenario

175   in which the sum of all cations (or anions) in the pore water is equal to the one of the injected

176    $KMnO_4$ solution. Scenarios "EK low" and "EK high" represent situations in which the sum of

177   cation equivalents in the background electrolyte solution is, respectively, three times lower and

178   three times higher than the concentration of the injected tracer. Upon application of an electric

179   field, the anions (including permanganate) move towards the anode on the right, whereas the

180   cations are transported towards the cathode on the left. Figure 1a shows a sketch of the

181   experimental setup and summarizes the injection and pore water concentrations in the different
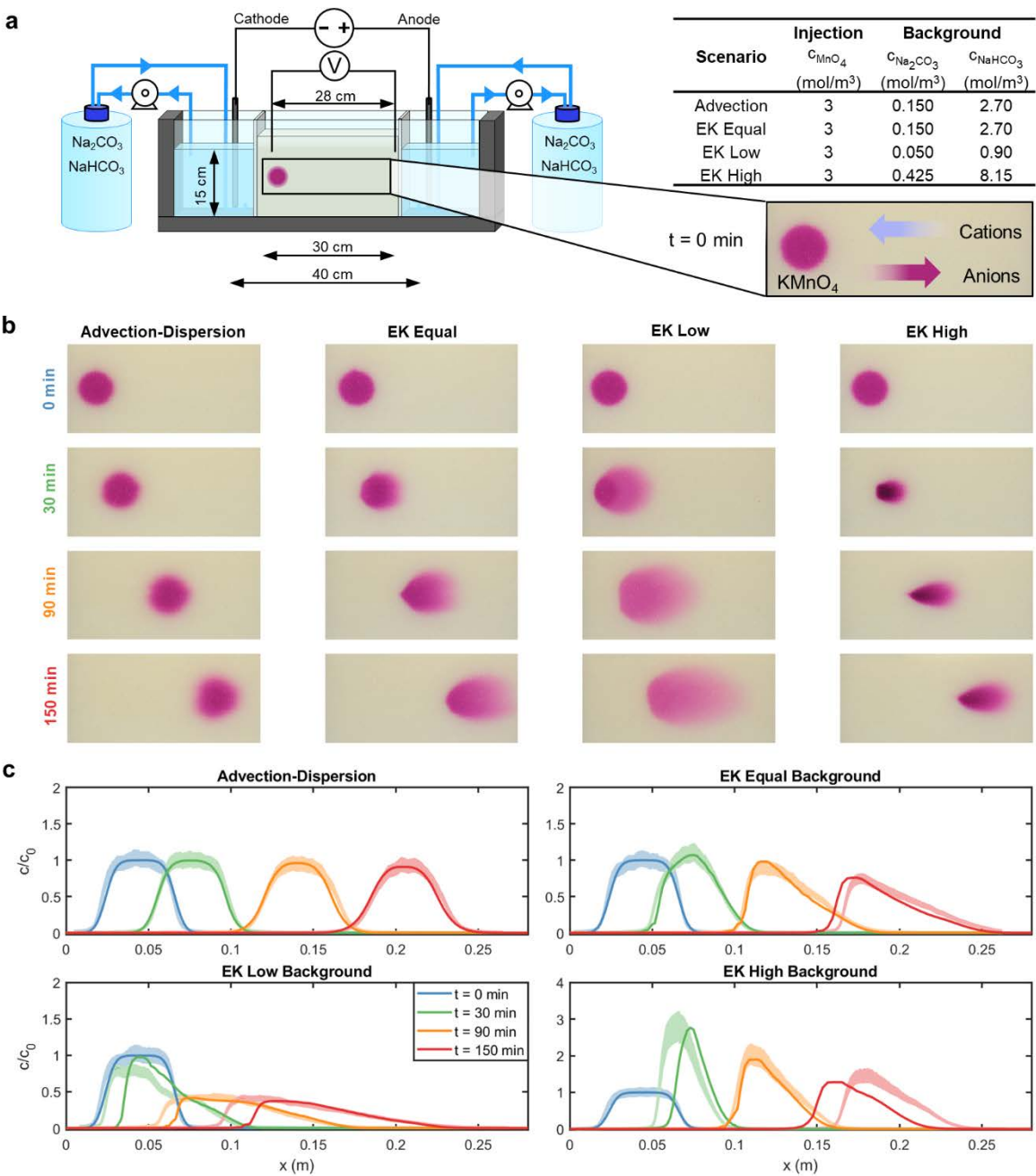
182   experiments.

Figure 1. *a Illustration of the experimental setup and summary of concentrations used in the different experiments. b images showing the evolution of the permanganate plume in the four different experiments. c concentration profiles evaluated through the longitudinal axis of the permanganate plume. The shaded area represents the experimental observations relating color intensity to concentration including uncertainty bands (±2σ), whereas the solid lines are the simulation outcomes.*

9

191

192   For every scenario we monitored the evolution of the tracer plume in the porous medium by

193   collecting pictures every minute for 150 minutes; Figure 1b presents four successive images of

194   each experiment. Considering the advection-dispersion case, the permanganate plume has a

195   regular and symmetric shape and moves with the water at the average linear pore water

196   velocity. Conversely, in the EK transport cases, although the nominal migration velocity is

197   comparable to the average pore water velocity in the advection-dispersion case, the shapes are

198   very different and the plumes appear to be substantially deformed with respect to the initial

199   circular shape. For instance, in scenario "EK equal", the permanganate plume becomes

200   elongated and a smooth concentration gradient develops at the front. A similar but more

201   pronounced behavior is observed for scenario "EK low", in which the permanganate plume has

202   a lower color intensity and is significantly more stretched in the longitudinal and transverse

203   directions. In contrast, in scenario "EK high", the permanganate plume initially contracts and

204   assumes a darker color. Successively, as the plume migrates towards the anode, it develops an

205   elongated shape parallel to the applied electric field. The velocity of plume displacement for

206   "EK equal" and "EK high" is similar and comparable with the advection-dispersion scenario.

207   In these cases, the center of mass of the plume has traveled a distance of approximately 150

208   mm after 150 min. The small electrolyte concentration in the case "EK low" has a clear effect

209   of retarding the plume. After 150 min and despite the application of the same electric potential

210   gradient, the centroid of the "EK low" plume has covered only 2/3 of the distance (~100 mm)

211   of the other plumes.

212   Figure 1c illustrates the longitudinal profiles of the MnO_4^- concentrations at different times.

213   Such profiles were evaluated both from the pictures, using a calibration function relating the

214   color intensity to the tracer concentration, and from the outcomes of a 2-D forward model,

215   describing the physical and electrostatic processes in the setup[36,37,39]. The simulation results,

216 showing the two-dimensional spatial distribution of the permanganate plumes at the different

217 times, are presented in Figure S4. In the first experimental scenario, with transport induced by

218 the hydraulic gradient, the permanganate concentration profiles are regular and follow the

219 classic theory of transport in porous media[40], as shown by the good agreement of the

220 experimental observations with the advection-dispersion simulations (Figure 1c). The transport

221 becomes radically different when MnO_4^- is displaced by electromigration. For instance, in the

222 "EK equal" experiment, the plume develops a smoother concentration front, whereas the back

223 of the plume presents a steep concentration profile even at late times. This behavior, inherently

224 dissimilar from advective-dispersive transport, can be simulated considering the charge

225 interactions and the coupled Nernst-Planck fluxes of the different charged species in the

226 domain.

227 The results of the numerical simulations allowed us to reproduce the experimental observations

228 very well, including the concentration values as well as the shape and the evolution of the

229 permanganate plume in the setup. In the scenario "EK low", the permanganate plume starts to

230 expand and slowly displaces with a lower concentration with respect to the previous scenarios.

231 The peak concentration (~ 1 mol/m^3) is in the order of the low background electrolyte

232 concentration in the pore water. Both the pictures and the longitudinal profiles also clearly

233 show a slower movement of the permanganate plume compared to the other experimental

234 scenarios. Conversely, in the scenario with high electrolyte background ("EK high"), the

235 concentration of the permanganate plume initially increases, with the highest value almost three

236 times the injected concentration. Successively, the plume migrates towards the anode with

237 similar velocity and smooth concentration fronts as in the scenario "EK equal".

238

239 *Charge interaction mechanisms*

240   Process-based numerical modeling is essential to mathematically describe electrokinetic

241   transport mechanisms, to visualize the spatial distribution of the delivered and of the

242   background charged species, to illuminate their coupled displacement and, ultimately, to allow

243   a quantitative interpretation of the experimental observations.

244   Figure 2a presents the simulated longitudinal concentration profiles of the different ions in the

245   experimental setup at the initial time and after 90 minutes. In the EK scenario with equal

246   background, MnO_4^- moves towards the anode, whereas K^+ exits the porous medium to the

247   cathode reservoir. In such scenario, the major background ions (sodium and bicarbonate) are

248   uniformly present in the domain at the beginning of the experiment, except in the area where

249   they were displaced by the injected $KMnO_4$ solution. Upon application of the electric potential,

250   HCO_3^- is transported towards the anode, in the same direction of MnO_4^-. At the same time, the

251   major cation in the system, Na^+, moves in the opposite direction towards the cathode. Note that

252   in every point, due to the condition of electroneutrality, the sum of equivalents of both cations

253   and anions must be the same. Consequently, the shape of the profiles of MnO_4^- and HCO_3^-

254   appear to be complementary as one anion can replace the other although together they cannot

255   exceed the charge that is carried by the cations in the same location. The smooth front of MnO_4^-

256   and the low concentration of HCO_3^- are mainly due to their different aqueous diffusion

257   coefficients (i.e., 1.50×10^{-9} for MnO_4^- and 1.09×10^{-9} for HCO_3^-). The higher diffusivity of

258   MnO_4^-, leads to its faster transport. However, such tendency is slowed down by the coupling

259   with HCO_3^-, which needs to be displaced and the overall charge in the system has to be

260   balanced. As a result, only a fraction of the permanganate front is able to proceed at the nominal

261   electromigration velocity imposed by the voltage difference at the electrodes, thus resulting in
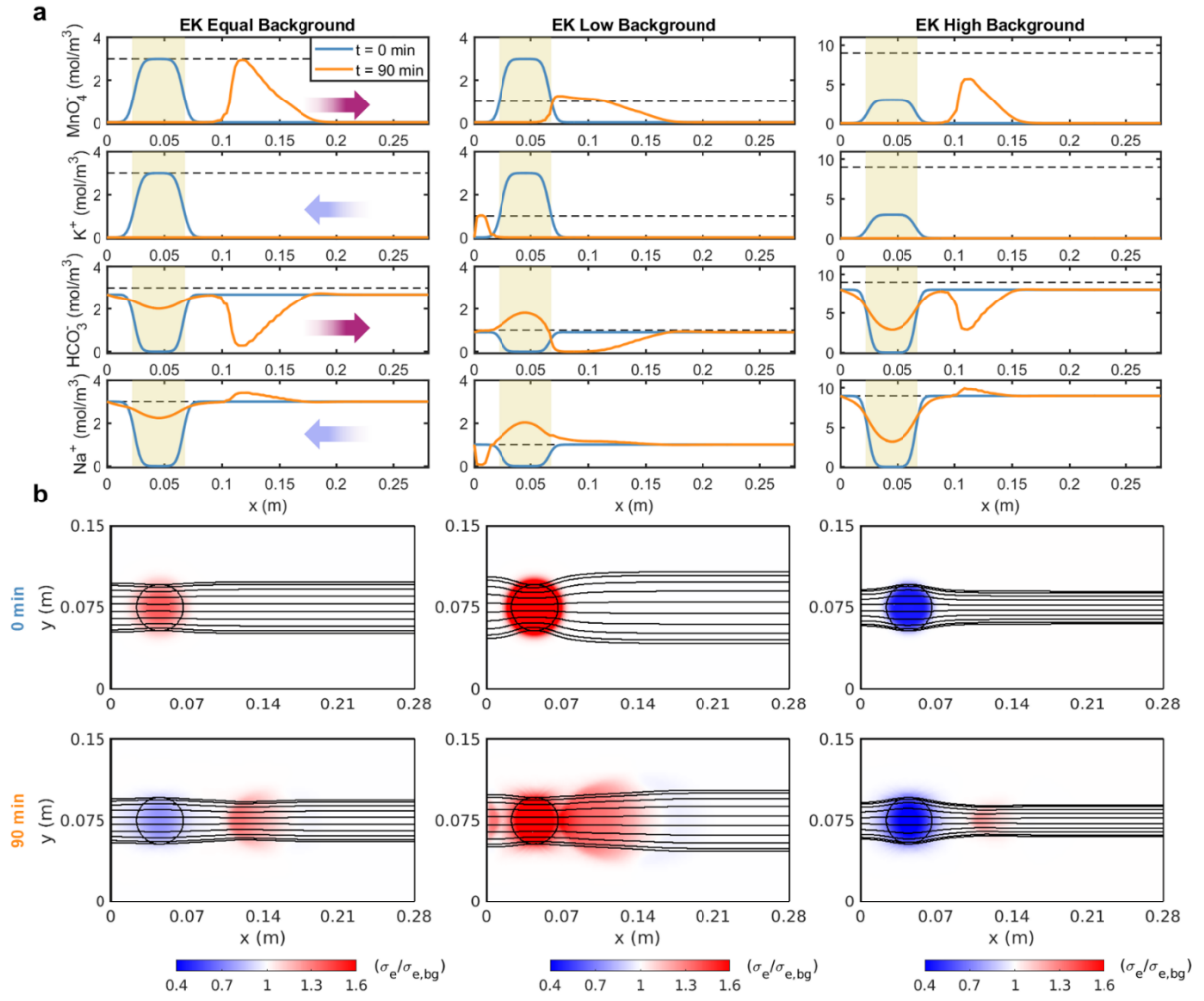
262   a smooth front progressively advancing in the domain.

263

Figure 2. *Simulated concentrations of major cations (Na^+ and K^+), anions (HCO_3^- and MnO_4^-) in the pore water and 2D electrolyte conductivity at different times. **a** cross-section illustrating the transport of the major ions in the system a t=0 and t=90 minutes for all three EK scenarios. The dashed lines represent the sum of all positive or negative charge equivalents in the system whereas the shaded area indicates the initial zone where the tracer has been injected. **b** normalized electrolyte conductivity maps with respect to the background conductivity for the three EK scenarios at t=0 and t=90 minutes (upper and bottom rows, respectively). The lines are the computed electric field streamlines passing through the central zone of the porous medium, where the tracer was injected.*

13

275   In the experiment with lower background ("EK low"), the concentration of MnO_4^- during

276   transport decreases significantly and approaches the values corresponding to the sum of the

277   equivalents of all cations in the background solution (dashed line in Figure 2a). This is the

278   result of the lower concentration of cations in the pore water, which limits the delivery of

279   permanganate. Only a fraction of the injected plume can enter the volume initially occupied by

280   the background electrolyte and starts to move towards the anode. The concentrations of Na^+

281   and HCO_3^- in the injection zone increases to fulfil the charge balance in this portion of the

282   domain where higher amounts of K^+ and MnO_4^- were initially injected. Finally, in the

283   experimental scenario with high background electrolyte ("EK high"), the increase of

284   permanganate concentration is the result of the high Na^+ present in the background (moving

285   towards the cathode), which requires a higher concentration of MnO_4^- (moving towards the

286   anode) to comply with the condition of electroneutrality. In this scenario, also the concentration

287   of both Na^+ and HCO_3^- after 90 minutes in the initial area of injection is similar to the initial

288   concentration of K^+ and MnO_4^-. Such situation is particularly interesting since the increase in

289   concentration, caused by electromigration fluxes (Figure S5) and resulting from the charge

290   interactions in the multicomponent ionic system, occurs against the natural concentration

291   gradient (Figure S6).

292   These experiments clearly show that the background electrolyte concentration controls the

293   mechanisms of electrokinetic transport and, thus, the delivery, the shape and the evolution of

294   the injected permanganate plumes. The driving force is indeed the electric potential gradient in

295   the system, which in turn is influenced by the electrolyte conductivity. The latter is a spatially

296   variable quantity in the considered setup, as illustrated in Figure 2b for all EK scenarios at t=0

297   and t=90 minutes. In scenario "EK equal", despite the concentrations of the background and

298   the tracer solutions are the same, the conductivity of the injected $KMnO_4$ plume is higher as a

299   result of the higher diffusivity of MnO_4^- and K^+ compared to the background ions. After 90

300 minutes, the distribution of MnO_4^- can be directly related to the electrolyte conductivity map

301 with a higher σ_e, whereas the injection zone still shows a lower value of σ_e due to the lower

302 diffusion coefficients of the background ions that occupied the injection's pore space. At this

303 later time, also the electric field streamlines are different and appear to focus on the area of the

304 permanganate plume, which has higher σ_e and has moved towards the anode. Similarly, in the

305 scenario with low background concentration, a strong focusing of the streamlines occurs in the

306 zone with initial injection of the plume where the higher σ_e results from the higher

307 concentration of the injected permanganate solution with respect to the background. This

308 phenomenon is due to the focusing of the electric field streamlines in zones with higher

309 electrolyte conductivity, where the intensity of the electric field is higher. Also in this case, a

310 subsequent defocusing of the streamlines causes a larger spreading of the permanganate plume.

311 At later times, the progressive distribution of the mass from the initial injection and the limiting

312 effect of the background electrolyte concentrations tend to suppress the differences in

313 conductivity.

314 For the scenario with high background electrolyte concentration, the streamlines show an

315 opposite pattern, first defocusing in the injection zone (low σ_e) and then focusing in the

316 direction of permanganate transport. In this case, it is possible to observe an increase of σ_e as

317 a result of the progressive increase in MnO_4^- concentration, as the permanganate plume shrinks

318 during its displacement towards the anode.

319 Overall, the computed 2D maps of electrolyte conductivity illustrate the evolution of this

320 property in the domain and the effects on the electric potential streamline patterns, which

321 directly affect the observed shape and propagation of the permanganate plume in the

322 experimental setup. Interestingly, during EK also the initial conditions of the system such as

323 local differences in σ_e between the injected tracer solution and the background are maintained

324 at later times and such effects only dissipate slowly as a result of diffusion.

325

Plume spreading and mixing

327   Transport of solutes in porous media results from complex pore-scale flow and mass transfer

328   processes that determine the macroscopic shape and evolution of injected plumes. Metrics

329   allowing the quantification of plume spreading and mixing are essential to describe solute

330   transport in porous domains[41,42]. The second central spatial moments, quantifying the mean

331   displacement of the concentration distribution from the plume centroid, are typically evaluated

332   to characterize plume spreading[43]. Here we determine the moments of the permanganate

333   plumes observed in our experiments as well as in the model simulations. To determine plume

334   mixing, instead, we use the concept of the dilution index, a metric based on the Shannon

335   entropy that quantifies the effective volume occupied by the plume[44]. Plume spreading and

336   mixing are evaluated for all conservative scenarios with the equations summarized in the

337   Supporting Information (Section S4). Figure 3a shows the permanganate plumes after 90

338   minutes from the injection for the four considered experimental scenarios. The pictures clearly

339   show different plume shape, mass distribution and solute concentration resulting from the

340   transport and electrostatic mechanisms in the experiments performed. The longitudinal and

341   transverse second central moments exhibit a distinct behavior in the experiments (Figure 3b).

342   In the advection-dispersion scenario, the longitudinal and transverse moments show a gradual

343   increase due to hydrodynamic dispersion at the plume fringes. In the EK scenario with the same

344   background concentration ("EK equal"), instead, the permanganate plume spreading is larger

345   both in the longitudinal and in the transverse directions. Spreading in both directions is very

346   pronounced in the experiment with low concentration of the background electrolyte in which

347   the observed permanganate concentrations are low and the plume spreads over a large portion

348   of the porous medium. The trends of the computed moments show higher slope at the

349   beginning, indicating that the spreading enhancement is more effective at early times. In the

350   scenario "EK high", the plume initially shrinks and then spreads. Such behavior is apparent

351   from the computed moments, showing decreasing values from the initial injection followed by

352   an increase as the plume is displaced towards the anode. The rate of increase is more

353   pronounced in the longitudinal direction, resulting in higher moments at late times compared

354   to the advection-dispersion case. For all the cases, the spatial moments from the 2-D

355   simulations allow capturing the trends computed from the experimental data.

356

357

358   *Figure 3. Metrics of spreading and mixing. **a** images of the permanganate plumes for the*

359   *different scenarios at t=90 minutes. **b** Second central spatial moments, dilution index and peak*

360   *concentration expressed as a function of time. The solid lines indicate model predictions*

361   *whereas the shaded areas represent the experimental results.*

362

363   Figure 3b also shows the evolution of the dilution index and the peak concentration of the

364   permanganate plumes. Such metrics are intrinsically related[44,45] and quantify the capability of

365   the injected plumes to effectively mix with the background pore water. In the advection-

366   dispersion case the dilution index shows a mild linear increase, as expected for transport in a

367   two-dimensional homogeneous porous medium, $E \sim t^{n/2}$, where n is the dimensionality of the

368   system[44]. Dilution appears to be stronger in the "EK equal" and "EK low" scenarios. In

369   particular, the latter case exhibits more than double increase in the plume dilution. These results

370   show the capability of EK transport to effectively distribute the mass of the injected tracer over

371   a larger pore water volume. Different, and perhaps even more interesting, is the case "EK high".

372   In such scenario the dilution index shows a non-monotonic trend with an initial decrease

373   (approximately half of the initial value during the first 30 minutes) followed by an increase to

374   a level similar to the dilution of the injected circular plume. The initial trend of the dilution

375   index of the MnO_4^- plume is counterintuitive based only on conventional mass transfer

376   mechanisms, since it indicates that the plume decreases its entropy. However, as explained

377   above, the plume shrinking, the peak concentration increase (almost three times the injected

378   values) and the dilution decrease are due to the electrostatic interactions with the ions present

379   at high concentration in the background pore water electrolyte and to the electroneutrality

380   constraint.

381

382   *Reactive transport experiments*

383   These experiments explored the displacement and degradation reaction of MnO_4^- under

384   advective-dispersive and electrokinetic transport. Permanganate was delivered in the porous

385   media with a background electrolyte containing glucose (8 mol/m^3) as model organic

386   compound. When these two reactants come into contact an oxidation-reduction reaction occurs,

387   which is described as a bimolecular reaction kinetics. In this set of reactive transport

388   experiments, the same EK scenarios with equal, low and high background concentration of

389   electrolytes were investigated and the results are illustrated in Figure 4.

390

Figure 4. *Reactive transport experiments and model analysis.* ***a*** *images showing the temporal evolution of the reactant plumes.* ***b*** *simulated reaction rates, considering a limiting threshold of 2×10^{-5} mol/m^3/s for all scenarios that allows the visualization of the different reaction patterns.* ***c*** *evaluation of the area for the mixing-controlled reaction and of the MnO_4^- mass simulated in the different scenarios.*

398   Figure 4a shows the evolution of the reactive system for the different scenarios over time. In

399   case of advection-dispersion, the reaction occurs at the fringe of the plume, where the

400   permanganate mixes with the glucose in the background pore water by hydrodynamic

401   dispersion. When the two solutes come into contact, the mixing-controlled reaction occurs. The

402   reaction area is visible from the pictures showing the formation of oxidation products at the

403   plume fringe and also from the numerical simulations. In this scenario the reactive fringe moves

404   with the permanganate plume in the same direction of the advective flow (Figure 4b).

405   In case of EK transport, the mixing mechanisms and the resulting patterns of reactants and

406   products distribution are completely different (Figure 4a-b). The applied electric field causes

407   the displacement of permanganate by electromigration but has no effect on the non-charged

408   glucose. Therefore, the mixing pattern resembles chromatographic mixing with an effective

409   overlap of the displaced permanganate with the immobile organic compound in the pore water.

410   The reactive zone is large, extending to the whole area of the plume, and is not restricted to a

411   thin fringe at the plume boundary. Indeed, in case of EK transport, more extensive degradation

412   and more effective consumption of permanganate are observed. It is also of interest to note the

413   effects of the different background electrolyte concentrations in the distinct EK reactive

414   transport experiments. When the electrolyte background solution has an equal concentration

415   with respect to the injected permanganate, the reaction occurs effectively and, after 150

416   minutes, almost all MnO_4^- has been consumed. In the case with low background electrolyte

417   concentration, the MnO_4^- plume spreads significantly and its concentration in the porous

418   medium is limited by the background electrolyte. Such behavior results in a large mixing area

419   but in a considerably slower reaction kinetics leading to only partial consumption of the

420   oxidant. Therefore, the slow kinetics of the redox reaction is the overall rate-limiting step,

421   resulting in the presence of a significant permanganate plume even after 150 minutes. Lastly,

422   in the experimental scenario with higher background concentration, the permanganate plume

20

423   shrinks and its concentration is increased. The mixing area is smaller but reactive mixing is

424   effective due to the higher concentration of MnO_4^- leading to faster reaction kinetics and to an

425   almost complete consumption of the permanganate plume.

426   Figure 4b illustrates the spatial and temporal distribution of the mixing-controlled reactive

427   zones in the different scenarios. The evolution of the computed mixing area and of the reaction

428   efficiency, quantified through the computed mass of permanganate in the domain, are shown

429   in Figure 4c. The mixing area is larger in the cases "EK equal" and "EK low" in which

430   permanganate electromigration and the composition of the background electrolyte solution lead

431   to an extended mixing zone. Such area of contact between the reactants reaches a maximum

432   and, successively, starts to decrease due to the consumption of the permanganate plume. The

433   mixing area is considerably more limited in the "Advection-Dispersion" and "EK high"

434   experiments. In these cases the values reached are similar but, as discussed above and

435   illustrated in Figure 4a-b, the shape of the mixing zone is completely different due to the

436   different transport mechanisms. Considering the degradation of the permanganate plumes upon

437   reaction with the glucose in the pore water, the simulations show nonlinear decreasing trends

438   of the remaining mass with significantly higher permanganate consumption in presence of

439   electrokinetic transport. In particular, the cases "EK equal" and "EK high" show the highest

440   efficiency and the lowest mass of permanganate in the system at the end of the simulation. In

441   these cases the simulation outcomes show that 75% of the initial permanganate mass was

442   consumed. A smaller efficiency (70% of the initial mass consumed) characterized the scenario

443   "EK low", whereas the lowest efficiency was observed in the advection-dispersion case in

444   which only 35% of the initial permanganate mass was consumed.

445

446   **Implications for electrokinetic applications**

447 Our investigation highlights important aspects and mechanisms of both scientific and practical

448 relevance for electrokinetic transport of charged species in porous media, which is of crucial

449 importance in different disciplines and has a wide range of current and potential applications

450 in geological, environmental, industrial and biological systems. We demonstrate that the pore

451 water chemistry and microscopic Coulombic interactions can both limit and/or enhance the

452 delivery of charged tracers by electrokinetics. The EK transport experiments performed clearly

453 show that when the background concentration of the cations or anions is significantly smaller

454 than an injected charged tracer, the tracer concentration that it possible to deliver by

455 electromigration is limited by the concentration level of the background electrolyte solution.

456 The ionic composition of the pore water also controls the tracer displacement, impacting the

457 movement of the center of mass as well as the shape and spreading of the plume both in

458 longitudinal and lateral directions. Moreover, the dilution of the injected tracer depends on the

459 background electrolyte that, when present at high concentration, can even lead to a decrease of

460 the dilution and the entropy of the plume and to an increase of its peak concentration. Of

461 environmental significance are also the outcomes of the reactive transport experiments showing

462 fascinating aspects of electrokinetically-induced charge species' mixing, leading to different

463 mass removal efficiencies and to quantitatively important effects of the pore water chemistry

464 on the kinetics of mixing-controlled degradation.

465 This investigation opens interesting perspectives on the possibility to employ microscopic

466 charge interactions to control macroscopic transport and to design innovative delivery

467 strategies in porous media that can be effectively implemented in practical applications, such

468 as soil and groundwater remediation. The mechanistic understanding of the fundamental role

469 of background electrolyte composition for the delivery of charged species during EK and the

470 developed process-based model, will allow the improvement of the performances of

471 electrokinetic distribution techniques for nutrients[39,46–48] and reactants[49–52] in subsurface

472   porous media. Specific examples include the quantitative assessment of the amounts and

473   distribution of delivered species, the optimization of voltage values, and the planning of

474   delivery strategies such as alternating active/inactive EK phases. Applications for subsurface

475   remediation encompass both low-permeability zones[25,26] but may also be employed to enhance

476   mixing and degradation of contaminant plumes in permeable aquifer systems, where poorly

477   mixing flow and transport regimes and mass transfer limitations[53] represent typical bottlenecks

478   to effective remediation. The detailed process knowledge obtained in this study will also be

479   instrumental for quantitative understanding of electrokinetic transport in heterogeneous porous

480   media, where high spatial variability of physical and chemical properties (e.g., permeability,

481   porosity, surface charge and pore water composition) will affect the electrokinetic delivery of

482   reactants, and where strong interactions between the different electrokinetic transport processes

483   will impact the effectiveness of in situ EK interventions. Finally, the combined experimental

484   and process-based modeling approach proposed in this study could be extended and further

485   developed for the use of different tracers and reactants, including micro- and nanomaterials for

486   subsurface remediation[54,55].

487

493

494   **Associated content**

495   *Supporting Information*

496   Details of the experimental setup, image analysis, governing equations, metrics of spreading,

497   dilution and mixing, and numerical modeling approach. 2-D model results of permanganate

498   transport at different times for the four conservative scenarios, simulated 2-D advective and

499   electromigration fluxes and diffusive/dispersive fluxes. Tables summarizing experimental

500   conditions (e.g., voltage, current, pH and temperature) and parameters used for the process-

501   based numerical modeling.

502

References

(1) Xie, X.; Ye, M.; Hsu, P. C.; Liu, N.; Criddle, C. S.; Cui, Y. Microbial Battery for Efficient Energy Recoèery. *Proc. Natl. Acad. Sci. U. S. A.* **2013**, *110* (40), 15925–15930. https://doi.org/10.1073/pnas.1307327110.

(2) Logan, B. E. Exoelectrogenic Bacteria That Power Microbial Fuel Cells. *Nat. Rev. Microbiol.* **2009**, *7*, 375–381. https://doi.org/10.1038/nrmicro2113.

(3) He, Z.; Minteer, S. D.; Angenent, L. T. Electricity Generation from Artificial Wastewater Using an Upflow Microbial Fuel Cell. *Environ. Sci. Technol.* **2005**, *39* (14), 5262–5267. https://doi.org/10.1021/es0502876.

(4) Friedmann, H.; Amiri, O.; Aït-Mokhtar, A.; Dumargue, P. A Direct Method for Determining Chloride Diffusion Coefficient by Using Migration Test. *Cem. Concr. Res.* **2004**, *34* (11), 1967–1973. https://doi.org/10.1016/j.cemconres.2004.01.009.

(5) Löfgren, M.; Neretnieks, I. Through-Electromigration: A New Method of Investigating Pore Connectivity and Obtaining Formation Factors. *J. Contam. Hydrol.* **2006**, *87* (3–4), 237–252. https://doi.org/10.1016/j.jconhyd.2006.05.006.

(6) Alkhadra, M. A.; Conforti, K. M.; Gao, T.; Tian, H.; Bazant, M. Z. Continuous Separation of Radionuclides from Contaminated Water by Shock Electrodialysis. *Environ. Sci. Technol.* **2019**, *54* (1), 527–536. https://doi.org/10.1021/acs.est.9b05380.

(7) Gabarrón, S.; Gernjak, W.; Valero, F.; Barceló, A.; Petrovic, M.; Rodríguez-Roda, I. Evaluation of Emerging Contaminants in a Drinking Water Treatment Plant Using Electrodialysis Reversal Technology. *J. Hazard. Mater.* **2016**, *309*, 192–201. https://doi.org/10.1016/j.jhazmat.2016.02.015.

(8) Patel, S. K.; Qin, M.; Walker, W. S.; Elimelech, M. Energy Efficiency of Electro-Driven Brackish Water Desalination: Electrodialysis Significantly Outperforms Membrane Capacitive Deionization. *Environ. Sci. Technol.* **2020**, *54* (6), 3663–3677. https://doi.org/10.1021/acs.est.9b07482.

(9) Sun, M.; Qin, M.; Wang, C.; Weng, G.; Huo, M.; Taylor, A. D.; Qu, J.; Elimelech, M. Electrochemical-Osmotic Process for Simultaneous Recovery of Electric Energy, Water, and Metals from Wastewater. *Environ. Sci. Technol.* **2020**, *54*, 8430–8442. https://doi.org/10.1021/acs.est.0c01891.

(10) Martens, E.; Prommer, H.; Dai, X.; Wu, M. Z.; Sun, J.; Breuer, P.; Fourie, A. Feasibility of Electrokinetic in Situ Leaching of Gold. *Hydrometallurgy* **2018**, *175*, 70–78. https://doi.org/10.1016/j.hydromet.2017.10.020.

(11) Guedes, P.; Couto, N.; Ottosen, L. M.; Ribeiro, A. B. Phosphorus Recovery from Sewage Sludge Ash through an Electrodialytic Process. *Waste Manag.* **2014**, *34* (5), 866–892. https://doi.org/10.1016/j.wasman.2014.02.021.

(12) Ribeiro, A. B.; Mateus, E. P.; Ottosen, L. M.; Bech-Nielsen, G. Electrodialytic Removal of Cu, Cr, and As from Chromated Copper Arsenate-Treated Timber Waste. *Environ. Sci. Technol.* **2000**, *34* (5), 784–788. https://doi.org/10.1021/es990442e.

(13) Probstein, R. F.; Hicks, R. E. Removal of Contaminants from Soils by Electric Fields. *Science (80-.).* **1993**, *260* (5107), 498–503. https://doi.org/10.1126/science.260.5107.498.

(14) Acar, Y. B.; Alshawabkeh, A. N. Principles of Electrokinetic Remediation. *Environ. Sci. Technol.* **1993**, *27* (13), 2638–2647. https://doi.org/10.1021/es00049a002.

(15) Cox, C. D.; Shoesmith, M. A.; Ghosh, M. M. Electrokinetic Remediation of Mercury-Contaminated Soils Using Iodine/Iodide Lixiviant. *Environ. Sci. Technol.* **1996**, *30* (6), 1933–1938. https://doi.org/10.1021/es950633r.

(16) Qin, J.; Sun, X.; Liu, Y.; Berthold, T.; Harms, H.; Wick, L. Y. Electrokinetic Control of Bacterial Deposition and Transport. *Environ. Sci. Technol.* **2015**, *49* (9), 5663–

552   5671. https://doi.org/10.1021/es506245y.

553   (17)   Shan, Y.; Harms, H.; Wick, L. Y. Electric Field Effects on Bacterial Deposition and
554   Transport in Porous Media. *Environ. Sci. Technol.* **2018**, *52* (24), 14294–14301.
555   https://doi.org/10.1021/acs.est.8b03648.

556   (18)   Wick, L. Y.; Mattle, P. A.; Wattiau, P.; Harms, H. Electrokinetic Transport of PAH-
557   Degrading Bacteria in Model Aquifers and Soil. *Environ. Sci. Technol.* **2004**, *38* (17),
558   4596–4602. https://doi.org/10.1021/es0354420.

559   (19)   Gill, R. T.; Harbottle, M. J.; Smith, J. W. N.; Thornton, S. F. Electrokinetic-Enhanced
560   Bioremediation of Organic Contaminants: A Review of Processes and Environmental
561   Applications. *Chemosphere* **2014**, *107*, 31–42.
562   https://doi.org/10.1016/J.CHEMOSPHERE.2014.03.019.

563   (20)   Tatti, F.; Papini, M. P.; Raboni, M.; Viotti, P. Image Analysis Procedure for Studying
564   Back-Diffusion Phenomena from Low-Permeability Layers in Laboratory Tests. *Sci.*
565   *Rep.* **2016**, *6* (July), 1–11. https://doi.org/10.1038/srep30400.

566   (21)   Chapman, S. W.; Parker, B. L. Plume Persistence Due to Aquitard Back Diffusion
567   Following Dense Nonaqueous Phase Liquid Source Removal or Isolation. *Water*
568   *Resour. Res.* **2005**, *41* (12). https://doi.org/10.1029/2005WR004224.

569   (22)   Sethi, R.; Molfetta, A. Di. *Groundwater Engineering - A Technical Approach to*
570   *Hydrogeology, Contaminant Transport and Groundwater Remediation*; Springer,
571   2019. https://doi.org/10.1016/0309-1708(88)90011-5.

572   (23)   Pamukcu, S. In Situ Soil and Sediment Remediation: Electrokinetic and
573   Electrochemical Methods. In *Handbook of Environmental Engineering*; Wiley Online
574   Library, 2018; pp 209–248.

575   (24)   Hodges, D.; Fourie, A.; Thomas, D.; Reynolds, D. Overcoming Permanganate Stalling
576   during Electromigration. *J. Environ. Eng.* **2013**, *139* (5), 677–684.
577   https://doi.org/10.1061/(ASCE)EE.1943-7870.0000660.

578   (25)   Reynolds, D. A.; Jones, E. H.; Gillen, M.; Yusoff, I.; Thomas, D. G. Electrokinetic
579   Migration of Permanganate through Low-Permeability Media. *Ground Water* **2008**, *46*
580   (4), 629–637. https://doi.org/10.1111/j.1745-6584.2008.00415.x.

581   (26)   Chowdhury, A. I. A.; Gerhard, J. I.; Reynolds, D.; Sleep, B. E.; O'Carroll, D. M.
582   Electrokinetic-Enhanced Permanganate Delivery and Remediation of Contaminated
583   Low Permeability Porous Media. *Water Res.* **2017**, *113*, 215–222.
584   https://doi.org/10.1016/j.watres.2017.02.005.

585   (27)   Poulson, S. R.; Naraoka, H. Carbon Isotope Fractionation during Permanganate
586   Oxidation of Chlorinated Ethylenes (CDCE, TCE, PCE). *Environ. Sci. Technol.* **2002**,
587   *36* (15), 3290–3274. https://doi.org/10.1021/es0205380.

588   (28)   Newman, J.; Thomas-Alyea, K. E. *Electrochemical Systems*; John Wiley & Sons,
589   2004.

590   (29)   Sprocati, R.; Rolle, M. Charge Interactions, Reaction Kinetics and Dimensionality
591   Effects on Electrokinetic Remediation: A Model-Based Analysis. *J. Contam. Hydrol.*
592   **2020**, *229*, 103567. https://doi.org/10.1016/j.jconhyd.2019.103567.

593   (30)   Rasouli, P.; Steefel, C. I.; Mayer, K. U.; Rolle, M. Benchmarks for Multicomponent
594   Diffusion and Electrochemical Migration. *Comput. Geosci.* **2015**, *19* (3), 523–533.
595   https://doi.org/10.1007/s10596-015-9481-z.

596   (31)   Zhang, L.; Wang, M. Modeling of Electrokinetic Reactive Transport in Micropore
597   Using a Coupled Lattice Boltzmann Method. *J. Geophys. Res. Solid Earth* **2015**, *120*
598   (5), 2877–2890. https://doi.org/10.1002/2014JB011812.

599   (32)   Wang, M.; Kang, Q.; Mukherjee, P. P.; Lichtner, P. C. Mesoscopic Modeling of
600   Multiphysicochemical Transport Phenomena in Porous Media. *Adv. Mech. Eng.* **2010**,
601   *2*. https://doi.org/10.1155/2010/142879.

602   (33)   Yang, Y.; Wang, M. Cation Diffusion in Compacted Clay: A Pore-Scale View.
603   *Environ. Sci. Technol.* **2019**, *53* (4), 1976–1984.
604   https://doi.org/10.1021/acs.est.8b05755.
605   (34)   MacGillivray, A. D. Nernst-Planck Equations and the Electroneutrality and Donnan
606   Equilibrium Assumptions. *J. Chem. Phys.* **1968**, *48* (7), 2903–2907.
607   https://doi.org/10.1063/1.1669549.
608   (35)   Sastre, M.; Santaballa, J. A. A Note on the Meaning of the Electroneutrality Condition
609   for Solutions. *J. Chem. Educ.* **1989**, *66* (5), 403. https://doi.org/10.1021/ed066p403.
610   (36)   Rolle, M.; Sprocati, R.; Masi, M.; Jin, B.; Muniruzzaman, M. Nernst-Planck-Based
611   Description of Transport, Coulombic Interactions, and Geochemical Reactions in
612   Porous Media: Modeling Approach and Benchmark Experiments. *Water Resour. Res.*
613   **2018**, *54* (4), 3176–3195. https://doi.org/10.1002/2017WR022344.
614   (37)   Sprocati, R.; Masi, M.; Muniruzzaman, M.; Rolle, M. Modeling Electrokinetic
615   Transport and Biogeochemical Reactions in Porous Media: A Multidimensional
616   Nernst-Planck-Poisson Approach with PHREEQC Coupling. *Adv. Water Resour.*
617   **2019**, *127*, 134–147. https://doi.org/10.1016/j.advwatres.2019.03.011.
618   (38)   Parkhurst, D. L.; Wissmeier, L. PhreeqcRM: A Reaction Module for Transport
619   Simulators Based on the Geochemical Model PHREEQC. *Adv. Water Resour.* **2015**,
620   *83*, 176–189. https://doi.org/10.1016/j.advwatres.2015.06.001.
621   (39)   Sprocati, R.; Flyvbjerg, J.; Tuxen, N.; Rolle, M. Process-Based Modeling of
622   Electrokinetic-Enhanced Bioremediation of Chlorinated Ethenes. *J. Hazard. Mater.*
623   **2020**, *397*, 122787. https://doi.org/10.1016/j.jhazmat.2020.122787.
624   (40)   Bear, J. *Dynamics of Fluids in Porous Media*; American Elsevier Publishing
625   Company, 1972. https://doi.org/10.1097/00010694-197508000-00022.
626   (41)   Hochstetler, D. L.; Rolle, M.; Chiogna, G.; Haberer, C. M.; Grathwohl, P.; Kitanidis,
627   P. K. Effects of Compound-Specific Transverse Mixing on Steady-State Reactive
628   Plumes: Insights from Pore-Scale Simulations and Darcy-Scale Experiments. *Adv.*
629   *Water Resour.* **2013**, *54*, 1–10. https://doi.org/10.1016/j.advwatres.2012.12.007.
630   (42)   Dentz, M.; Le Borgne, T.; Englert, A.; Bijeljic, B. Mixing, Spreading and Reaction in
631   Heterogeneous Media: A Brief Review. *J. Contam. Hydrol.* **2011**, *120*, 1–17.
632   https://doi.org/10.1016/j.jconhyd.2010.05.002.
633   (43)   Kitanidis, P. K. Analysis of Macrodispersion through Volume-Averaging: Moment
634   Equations. *Stoch. Hydrol. Hydraul.* **1992**, *6* (1), 5–25.
635   https://doi.org/10.1007/BF01581672.
636   (44)   Kitanidis, P. K. The Concept of the Dilution Index. *Water Resour. Res.* **1994**, *30* (7),
637   2011–2026. https://doi.org/10.1029/94WR00762.
638   (45)   Rolle, M.; Kitanidis, P. K. Effects of Compound-Specific Dilution on Transient
639   Transport and Solute Breakthrough: A Pore-Scale Analysis. *Adv. Water Resour.* **2014**,
640   *71*, 186–199. https://doi.org/10.1016/j.advwatres.2014.06.012.
641   (46)   Mao, X.; Wang, J.; Ciblak, A.; Cox, E. E.; Riis, C.; Terkelsen, M.; Gent, D. B.;
642   Alshawabkeh, A. N. Electrokinetic-Enhanced Bioaugmentation for Remediation of
643   Chlorinated Solvents Contaminated Clay. *J. Hazard. Mater.* **2012**.
644   https://doi.org/10.1016/j.jhazmat.2012.02.001.
645   (47)   Gill, R. T.; Thornton, S. F.; Harbottle, M. J.; Smith, J. W. Effect of Physical
646   Heterogeneity on the Electromigration of Nitrate in Layered Granular Porous Media.
647   *Electrochim. Acta* **2016**, *199*, 59–69. https://doi.org/10.1016/j.electacta.2016.02.191.
648   (48)   Schmidt, C. A. B.; Barbosa, M. C.; de Almeida, M. de S. S. A Laboratory Feasibility
649   Study on Electrokinetic Injection of Nutrients on an Organic, Tropical, Clayey Soil. *J.*
650   *Hazard. Mater.* **2007**, *143* (3), 665–661.
651   https://doi.org/10.1016/j.jhazmat.2007.01.009.

652 (49) Chowdhury, A. I. A.; Gerhard, J. I.; Reynolds, D.; O'Carroll, D. M. Low Permeability
653   Zone Remediation via Oxidant Delivered by Electrokinetics and Activated by
654   Electrical Resistance Heating: Proof of Concept. *Environ. Sci. Technol.* **2017**, *51* (22),
655   13295–13303. https://doi.org/10.1021/acs.est.7b02231.

656 (50) Wu, M. Z.; Reynolds, D. A.; Fourie, A.; Prommer, H.; Thomas, D. G. Electrokinetic in
657   Situ Oxidation Remediation: Assessment of Parameter Sensitivities and the Influence
658   of Aquifer Heterogeneity on Remediation Efficiency. *J. Contam. Hydrol.* **2012**, *136–*
659   *137*, 72–85. https://doi.org/10.1016/j.jconhyd.2012.04.005.

660 (51) Fan, G.; Cang, L.; Gomes, H. I.; Zhou, D. Electrokinetic Delivery of Persulfate to
661   Remediate PCBs Polluted Soils: Effect of Different Activation Methods. *Chemosphere*
662   **2016**, *144*, 138–147. https://doi.org/10.1016/j.chemosphere.2015.08.074.

663 (52) Head, N. A.; Gerhard, J. I.; Inglis, A. M.; Nunez Garcia, A.; Chowdhury, A. I. A.;
664   Reynolds, D. A.; de Boer, C. V.; Sidebottom, A.; Austrins, L. M.; Eimers, J.;
665   O'Carroll, D. M. Field Test of Electrokinetically-Delivered Thermally Activated
666   Persulfate for Remediation of Chlorinated Solvents in Clay. *Water Res.* **2020**, *183*
667   (15), 116061. https://doi.org/10.1016/j.watres.2020.116061.

668 (53) Rolle, M.; Chiogna, G.; Hochstetler, D. L.; Kitanidis, P. K. On the Importance of
669   Diffusion and Compound-Specific Mixing for Groundwater Transport: An
670   Investigation from Pore to Field Scale. *J. Contam. Hydrol.* **2013**, *153*, 51–68.
671   https://doi.org/10.1016/j.jconhyd.2013.07.006.

672 (54) Velimirovic, M.; Bianco, C.; Ferrantello, N.; Tosco, T.; Casasso, A.; Sethi, R.;
673   Schmid, D.; Wagner, S.; Miyajima, K.; Klaas, N.; Meckenstock, R. U.; von der
674   Kammer, F.; Hofmann, T. A Large-Scale 3D Study on Transport of Humic Acid-
675   Coated Goethite Nanoparticles for Aquifer Remediation. *Water* **2020**, *12* (4), 1207.
676   https://doi.org/10.3390/W12041207.

677 (55) Czinnerová, M.; Vološčuková, O.; Marková, K.; Ševců, A.; Černík, M.; Nosek, J.
678   Combining Nanoscale Zero-Valent Iron with Electrokinetic Treatment for
679   Remediation of Chlorinated Ethenes and Promoting Biodegradation: A Long-Term
680   Field Study. *Water Res.* **2020**, *175* (15), 115692.
681   https://doi.org/10.1016/j.watres.2020.115692.

682